

Topology detection in cavity QED

Beatriz Pérez-González,¹ Álvaro Gómez-León,² and Gloria Platero¹

¹*Instituto de Ciencia de Materiales de Madrid (ICMM, CSIC)*

²*Instituto de Física Fundamental (IFF, CSIC)*

We explore the physics of topological lattice models in c-QED architectures for arbitrary coupling strength, and the use of the cavity transmission as a topological marker. For this, we develop an approach combining the input-output formalism with an expansion in quantum fluctuations which allows to go beyond the small-coupling regime. We apply our formalism to a fermionic Su-Schrieffer-Heeger (SSH) chain coupled to a single-mode cavity, and find that the cavity can indeed act as a quantum sensor for topological phases, where the initial state preparation plays a crucial role. Additionally, we discuss the persistence of topological features as the coupling strength increases, in terms of an effective Hamiltonian, and calculate the entanglement entropy.

Introduction. – Cavity Quantum Electro-Dynamics (c-QED) studies the interaction between light and matter at the most elementary level, either with individual atoms [1] or solid-state devices [2]. These hybrid systems have revealed themselves as an important tool for the control of quantum systems [3], and an essential landmark in the development of quantum technologies [4–6]. This is because the coherent interaction of both systems allows for an efficient transfer of information between the two [7, 8], provided that their coupling is larger than the losses in the system.

A step further can be taken by considering the combination of quantum light and complex quantum materials, such as topological systems [9–12]. A celebrated example of such are topological insulators (TIs), which have mid-gap states which are exponentially localized at the boundaries and protected by certain symmetries of the band structure.

In this work, we study the interplay of fermionic topological systems and c-QED architectures. Our aim is to use the cavity transmission as a topological marker, identifying the experimental signatures of non-trivial topological properties. For that purpose, we develop a framework combining input-output theory with an expansion in quantum fluctuations whose validity extends to arbitrary coupling strength. Finally, we study in detail the case of the SSH chain [13–15] coupled to a single mode cavity.

Mean-field and Fluctuations Hamiltonian. – We consider the Hamiltonian $H = \Omega d^\dagger d + H_S + V$. The first term describes a cavity with frequency Ω , being d (d^\dagger) the destruction (creation) photon operator, while H_S corresponds to the single-particle Hamiltonian of a topological system. The interaction term has the form $V = g(d^\dagger + d)Z$, being Z the fermionic coupling operator and g the coupling strength.

We apply a mean-field (MF) decoupling and write each operator in V as its average plus the fluctuations around it: $\mathcal{O} = \langle \mathcal{O} \rangle + \delta\mathcal{O}$, being $\delta\mathcal{O}$ the fluctuations opera-

tor. Then, we identify two contributions: i) the MF Hamiltonian, which is linear in fluctuations and can be described by $\tilde{H}_S = H_S + g(\langle d^\dagger \rangle + \langle d \rangle)Z$ for fermions, and $H_\Omega = \Omega d^\dagger d + g\langle Z \rangle(d^\dagger + d)$ for photons; and ii) the quadratic part in fluctuations $H_\delta = g(\delta d^\dagger + \delta d)\delta Z$. Note that the MF part is written in terms of the original operators using $\delta\mathcal{O} = \mathcal{O} - \langle \mathcal{O} \rangle$, and that constant terms have been neglected.

Finally, a complete characterization requires self-consistent solutions to $\langle Z \rangle$, $\langle d^\dagger \rangle$ and $\langle d \rangle$, which can be obtained, to lowest order, from the MF Hamiltonian. This requires to rotate H_Ω with $R = \exp\{-g\langle Z \rangle(d^\dagger - d)/\Omega\}$, to find:

$$\tilde{H}_\Omega = R^\dagger H_\Omega R = \Omega d^\dagger d - \frac{g^2 \langle Z \rangle^2}{\Omega}. \quad (1)$$

Importantly, \tilde{H}_Ω is now diagonal in the rotated basis, where it is easy to determine the average of the photon operators: $\langle d^\dagger \rangle + \langle d \rangle = -2g\langle Z \rangle/\Omega$. We can then write \tilde{H}_S in terms of fermionic averages only:

$$\tilde{H}_S = H_S - 2\frac{g^2}{\Omega}\langle Z \rangle Z. \quad (2)$$

Notice that the interaction with the cavity photons introduces a term proportional to Z , that can affect the topological properties of \tilde{H}_S . Fortunately, Eq. 2 simplifies the calculation of $\langle Z \rangle$, which can now be obtained using an iterative numerical procedure involving fermionic degrees of freedom only. Finally, \tilde{H}_δ can also be written in the rotated frame:

$$\tilde{H}_\delta = R^\dagger H_\delta R = g(d^\dagger + d) \sum_{\tilde{\alpha}} \tilde{Z}_{\tilde{\alpha}} \tilde{X}^{\tilde{\alpha}}, \quad (3)$$

where $\tilde{Z}_{\tilde{\alpha}} = \langle \tilde{\alpha}_1 | (Z - \langle Z \rangle) | \tilde{\alpha}_2 \rangle$, and we define the Hubbard operators $\tilde{X}^{\tilde{\alpha}} = \tilde{X}^{\alpha_1, \alpha_2} = |\tilde{\alpha}_1\rangle\langle \tilde{\alpha}_2|$,

with $|\tilde{\alpha}_i\rangle$ ($\alpha_i = 1, \dots, N$) being the eigenstates of $\tilde{H}_S|\tilde{\alpha}_i\rangle = \tilde{E}_{\alpha_i}|\tilde{\alpha}_i\rangle$, and $\tilde{\alpha} = (\alpha_1, \alpha_2)$. Indeed, $\tilde{Z}_{\tilde{\alpha}}$ measures the effect of fluctuations on the MF eigenstates: it vanishes in the two asymptotic limits $g \ll \Omega, \tilde{E}_{\tilde{\alpha}}$ and $g \gg \Omega, \tilde{E}_{\tilde{\alpha}}$, implying that fluctuations are completely suppressed in the rotated frame, where the two systems effectively decouple, making the MF description exact. Away from these limits, fluctuations are relevant and must be estimated.

Calculation of the cavity transmission. – To study the cavity transmission t_c , we include the coupling of the cavity photons to the external modes [16]. By means of input-output theory, we can obtain the input $\tilde{b}_{\text{in},l}$ and output $\tilde{b}_{\text{out},l}$ fields at each of the sides $l = 1, 2$ of the cavity, and write $t_c = |t_c|e^{i\varphi} = \langle \tilde{b}_{\text{out}} \rangle / \langle \tilde{b}_{\text{in}} \rangle$ [17].

The starting point is the Langevin equation of motion (EoM) for the cavity field $d(t)$ [4, 16]:

$$\partial_t d(t) = -i \left(\Omega - i \frac{\kappa}{2} \right) d(t) - \sum_{l=1,2} \sqrt{\kappa_l} \tilde{b}_{\text{in},l}(t) - ig \sum_{\tilde{\alpha}} \tilde{Z}_{\tilde{\alpha}} \tilde{X}^{\tilde{\alpha}}(t), \quad (4)$$

where κ_l represents the coupling between the cavity and the outside modes, and $\kappa = \kappa_1 + \kappa_2$. To solve it, we consider the retarded Green function $G(t, t') = -i\theta(t - t')\langle [d(t), d^\dagger(t')] \rangle$. Considering its Langevin EoM with local dissipation κ , obtained from the quantum regression theorem, we notice that the EoM for $G(t, t')$ is analogous to Eq. 4, but without the term $\sqrt{\kappa_l} \tilde{b}_{\text{in}}$. Then, it is only required to notice that $G(t, t')$ is the resolvent of Eq. (4), which means we can write a general solution for $d(\omega)$ as $d(\omega) = -iG(\omega) \sum_{l=1,2} \sqrt{\kappa_l} \tilde{b}_{\text{in},l}(\omega)$ for arbitrary g [17]. Together with the input-output relation $\tilde{b}_{\text{out},l}(t) = \tilde{b}_{\text{in},l}(t) + \sqrt{\kappa_l} d(t)$ (obtained from the reversed-time EoM for $d(\omega)$), this result let us write

$$t_c(\omega) = \frac{\langle \tilde{b}_{\text{out},2} \rangle}{\langle \tilde{b}_{\text{in},1} \rangle} = -i\sqrt{\kappa_1 \kappa_2} G(\omega), \quad (5)$$

To connect with the standard input-output result for t_c , the EoM for $G(\omega)$ can be solved, using

$$\partial_t \tilde{X}^{\tilde{\alpha}}(t) = i \left(\tilde{E}_{\tilde{\alpha}} - i \frac{\gamma}{2} \right) \tilde{X}^{\tilde{\alpha}}(t) + ig [d^\dagger(t) + d(t)] Y_{\tilde{\alpha}}^-(t) \quad (6)$$

where $Y_{\tilde{\alpha}}^-(t) = \sum_{\beta} (\tilde{Z}_{\alpha_2 \beta} \tilde{X}^{\alpha_1 \beta}(t) - \tilde{Z}_{\beta \alpha_1} \tilde{X}^{\beta \alpha_2}(t))$, $\tilde{E}_{\tilde{\alpha}} = \tilde{E}_{\alpha_1} - \tilde{E}_{\alpha_2}$, and γ is the spectral broadening. To close the system of equations, a decoupling scheme is required. For this, we notice that contributions from fluctuations are small for $g \ll \Omega, \tilde{E}_{\tilde{\alpha}}$ and $g \gg \Omega, \tilde{E}_{\tilde{\alpha}}$, when working in the rotating frame. Under these conditions, we

can rewrite $d^{(\dagger)}(t) \tilde{X}^{\tilde{\alpha}}(t) \approx \langle \tilde{X}^{\tilde{\alpha}} \rangle d^{(\dagger)}(t) + \langle d^{(\dagger)} \rangle \tilde{X}^{\tilde{\alpha}}(t)$. Note that we are also neglecting extra correlation terms between photonic and fermionic operators by assuming that fluctuations are small, which would only be relevant near resonances. For the same reason, $\langle d^{(\dagger)} \rangle$ and $\langle \tilde{X} \rangle$ can be calculated using \tilde{H}_Ω and \tilde{H}_S , respectively. As a result, $\langle d^{(\dagger)} \rangle \sim 0$ in the rotated frame. We will also neglect $\langle \tilde{X} \rangle d^\dagger(t)$ for being small in the regime of interest [18].

With these approximations, we can solve the EoM for $G(\omega)$ and obtain an analytical expression for t_c :

$$t_c = \frac{\langle \tilde{b}_{\text{out},2} \rangle}{\langle \tilde{b}_{\text{in},1} \rangle} = \frac{i\sqrt{\kappa_1 \kappa_2}}{\Omega - \omega + g^2 \tilde{\chi}(\omega) - i \frac{\kappa}{2}} \quad (7)$$

where $\tilde{\chi}(\omega)$ is the electronic susceptibility,

$$\tilde{\chi}(\omega) = \sum_{\tilde{\alpha}\beta} \tilde{Z}_{\tilde{\alpha}} \frac{\tilde{Z}_{\alpha_2, \beta} \langle \tilde{X}^{\alpha_1, \beta} \rangle - \tilde{Z}_{\beta, \alpha_1} \langle \tilde{X}^{\beta, \alpha_2} \rangle}{\omega + \tilde{E}_{\tilde{\alpha}} - i \frac{\gamma}{2}} \quad (8)$$

with $\langle \tilde{X}^{\tilde{\alpha}} \rangle = \delta_{\alpha_1, \alpha_2} p_{\alpha_1}$, being p_α the occupation of state $|\tilde{\alpha}\rangle$ in the fermionic density matrix $\rho_f = \sum_{\alpha} p_\alpha \tilde{X}^{\alpha, \alpha}$. Eq. 8 is analogous to the electronic susceptibility for the small- g regime in the standard input-output formalism [18], but in this case all fermionic parameters are renormalized by the MF self-consistency equations. This allows to extend the validity of Eq. 7 to the very-large- g regime, but we will see below that it also reproduces the behaviour in the intermediate regime accurately.

Results. – The theoretical framework developed so far can be used for an arbitrary H_S and Z . Now we apply our formalism to a particular fermionic 1D topological system described by $H_S = \sum_{(i,j)=1}^N t_{ij} c_i^\dagger c_j$, where t_{ij} is the hopping amplitude and c_i (c_i^\dagger) is the destruction (creation) operator for a spinless fermion at site i ($i = 1, \dots, N$). Particularizing for the SSH model [13–15], we define the intra- and inter-dimer hopping amplitudes $t = t_0(1 + \delta)$ and $t' = t_0(1 - \delta)$, respectively, with $\delta \in [-1, 1]$. This bipartite structure gives rise to two distinct topological phases: the trivial phase ($\delta < 0$), and the topological phase ($\delta > 0$), hosting a pair of topologically protected edge states. In the following, we set $t_0 \equiv 1$ as the energy scale for Ω and g .

For the interaction between the cavity and the chain we consider the dipolar coupling, $Z = \sum_i x_i c_i^\dagger c_i$ [19], being x_i the position in the lattice such that $x_N = -x_1$. We have calculated $\langle Z \rangle$ vs g self consistently and found that for small g , $\langle Z \rangle = 0$ (see details in [17]). This confirms that the eigenstates of \tilde{H}_S coincide with those of H_S ($\tilde{E}_{\tilde{\alpha}} \rightarrow E_{\tilde{\alpha}}$, $\tilde{X}^{\tilde{\alpha}} \rightarrow X^{\tilde{\alpha}}$) and \tilde{H}_δ turns into the original V (i.e. $\tilde{Z} \rightarrow Z$).

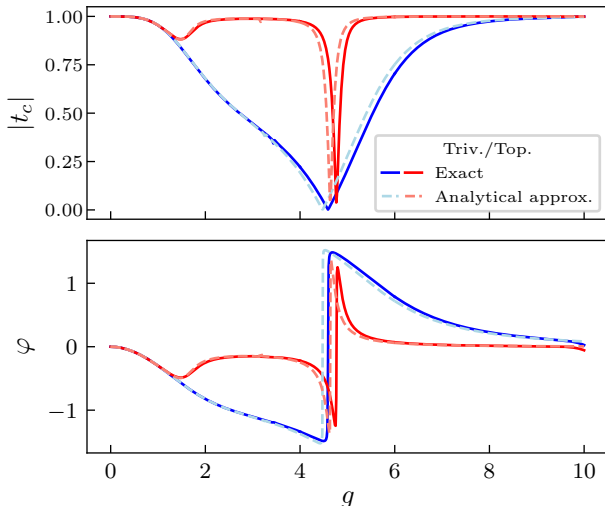


Figure 1: $|t_c(\Omega)|$ and φ vs g . Dashed lines correspond to the analytical approximation (Eq. 7), and solid lines to the exact solution (Eq. 5). The ground state of the chain is occupied. Parameters: $\omega = \Omega = 10, \delta = \pm 0.6, N = 20, \gamma = \kappa_1 = \kappa_2 = 0.01$.

In this regime, $Z_{\bar{\alpha}}$ mediates transitions between all eigenstates of the chain, with the exception of the edge states in the topological phase, which exponentially suppress their coupling with the bulk states as a function of the chain length. In consequence, if the system is initially prepared in its ground state, the interaction with the electronic system will shift the cavity frequency equally for both phases, which means that t_c cannot be used as a topological marker in this regime, and only the initial preparation in an edge state would allow to detect topology [17]. In contrast, $\langle Z \rangle \neq 0$ for $g \gg \Omega, |t_{i,j}|$, accounting for the polarization of the system. However, the global shift in the energy of the cavity photons does not affect the measurement of t_c , so we expect $|t_c| \simeq 1$ again.

All these features are shown in Fig. 1, where we have calculated t_c at $\omega = \Omega = 10$ (highly detuned from the electronic system) for both phases, as a function of g , including from the small to the very-large g regime. We consider *the chain with one particle in its lowest energy state*. For small g , the peak of maximum transmission, initially found at $\omega = \Omega$, shifts due to the interaction for both phases. The edge states are transparent to the bulk states and their presence is not revealed in t_c . However, Eqs. 7 and 5 predict that the break-down of the small- g regime brings essential differences between phases: while the trivial phase decays monotonically until reaching a minimum, the topological phase remains mostly unaffected, except for a notorious dip in $|t_c|$ (which corresponds to a change of sign in φ). Thus, the effect of the topological edge states is not washed away by the chiral-symmetry breaking, and the difference between phases

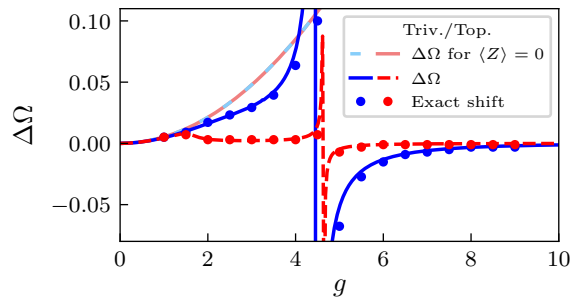


Figure 2: Plot of $\Delta\Omega$ (Eq. 10) vs g for both the trivial (blue) and topological (red) phase. The comparison with $\Delta\Omega$ calculated with $\langle Z \rangle$ has been included in lighter colors. The dots corresponds to the exact shift (Eq.5). Parameters: $\Omega = 10, \delta = \pm 0.6, N = 20$

can still be detected. Finally, both phases display perfect transmission when g is sufficiently large, in accordance with the MF analysis. Importantly, the comparison between Eqs. 7 and 5 gives a perfect agreement between the exact and the analytical curves for arbitrary g , which means that Eq. 7 captures the behaviour of the system for arbitrary coupling.

Effective Hamiltonian. – To explore in more detail the different interaction regimes, we derive an effective Hamiltonian using a Schrieffer-Wolff transformation in the basis of eigenstates of the MF Hamiltonian, where \tilde{H}_δ is considered the perturbation to $\tilde{H}_S + \tilde{H}_\Omega$. The transformation is defined through the generator S such that $\bar{H} = e^S \tilde{H} e^{-S} \simeq \tilde{H}_S + \tilde{H}_\Omega + \frac{1}{2} [S, \tilde{H}_\delta]$, yielding [17]

$$\bar{H} \simeq \sum_{i,j} \tilde{E}_i \tilde{X}^{ii} + \left[\Omega + g^2 \sum_{\bar{\alpha}} \tilde{\Omega}_{\bar{\alpha}} \tilde{Y}_{\bar{\alpha}}^- \right] d^\dagger d + \frac{g^2}{2} \sum_{\bar{\alpha}} \tilde{Z}_{\bar{\alpha}} \sum_{\beta} \left[\frac{\tilde{Z}_{\alpha_2 \beta} \tilde{X}^{\alpha_1 \beta}}{\tilde{E}_{\bar{\alpha}} - \Omega} - \frac{\tilde{Z}_{\beta \alpha_1} \tilde{X}^{\beta \alpha_2}}{\tilde{E}_{\bar{\alpha}} + \Omega} \right] \quad (9)$$

with $\tilde{\Omega}_{\bar{\alpha}} = \tilde{Z}_{\bar{\alpha}} \tilde{E}_{\bar{\alpha}} / (\tilde{E}_{\bar{\alpha}}^2 - \Omega^2)$. To derive Eq.9 we have neglected the small correction provided by two-photon transitions in the rotated frame. Then, \bar{H} includes a shift in the cavity frequency Ω , proportional to $\tilde{\Omega}_{\bar{\alpha}}$, that depends on the state of the electronic system through $\tilde{Z}_{jn} \langle \tilde{X}^{in} \rangle - \tilde{Z}_{ni} \langle \tilde{X}^{nj} \rangle$, as well as a correction to the MF electronic energies (second line).

The total frequency shift can be obtained from $\Delta\Omega = g^2 \sum_{ij} \tilde{\Omega}_{ij} \left(\tilde{Z}_{jn} \langle \tilde{X}^{in} \rangle - \tilde{Z}_{ni} \langle \tilde{X}^{nj} \rangle \right)$, where the expected values are calculated to lowest order using the ground state of \tilde{H}_S . In this case, $\Delta\Omega$ reduces to:

$$\Delta\Omega = g^2 \sum_j |\tilde{Z}_{0j}|^2 \frac{\tilde{E}_0 - \tilde{E}_j}{(\tilde{E}_0 - \tilde{E}_j)^2 - \Omega^2}. \quad (10)$$

Fig. 2 shows $\Delta\Omega$ vs g for the same parameters as Fig. 1. Dots correspond to the exact shift obtained from Eq.5, exhibiting an excellent agreement with the predictions from \tilde{H} for arbitrary g . For larger g , Eq. 10 also captures the presence of a divergence (signaling a resonance between photons and fermions), in accordance with the drop in t_c shown in Fig. 1 for both phases. Additionally, $\Delta\Omega$ obtained for $\langle Z \rangle = 0$ ($\tilde{Z} \rightarrow Z$, $\tilde{E}_i \rightarrow E_i$) has been included. These results indicate that: i) the dependence of \tilde{H}_S on $\langle Z \rangle$ makes Eqs. 5 and 9 non-perturbative, since $\langle Z \rangle$ is also a function of the other parameters; and ii) the polarization of the system with $\langle Z \rangle \neq 0$ triggers the onset of the qualitatively distinct behaviour between both phases (Fig. 1) and the breakdown of the small- g regime, enabling topological detection for equilibrium configurations (i.e. ground state occupied). Also note in Fig. 2 that $\Delta\Omega$ changes sign after the divergence. Finally, for $g \gtrsim \Omega$, $\delta\Omega \rightarrow 0$ for both phases, as expected: fluctuations are suppressed and there is a global shift in the energy of the photons (Eq. 1), not detected in t_c .

The change in the eigenenergies of the system due to the interaction is not trivial. The polarization of the system with $\langle Z \rangle \neq 0$ introduces an on-site energy (Eq. 2), which localizes the states and breaks the original chiral symmetry of the SSH model. However, the breaking of the symmetries that provide for topological protection is expected even for small g due to the term in the second line of Eq. 9. Indeed, as g increases, the topological edge states reduce their energy and eventually penetrate into the bulk band. Despite this, their presence can be detected in t_c , even after their disappearance, thus accounting for the differences in t_c between phases. Besides, this correction to the electronic MF eigenstates can be used to measure the effect of fluctuations on the ground state of \tilde{H}_S . A numerical estimation reveals that it is very small even in the intermediate regime, which explains why there is such a good agreement between the exact (Eq. 5) and analytical (Eq. 7) t_c for arbitrary g Fig. 1.

Entanglement entropy. – To gain further insight into the topological features of the intermediate coupling regime, we explore the entanglement entropy $S_A = -\text{tr}_A \rho_A \ln \rho_A$, where ρ_A corresponds to the reduced density matrix of a subsystem A . When the system is divided in two partitions $A \oplus B$, S_A measures the amount of quantum correlation between them (note that $S_A = S_B$, with S_B defined analogously).

We can partition the system in two different ways. First, we consider a partition separating the fermionic chain and the cavity, and calculate S_{e1} by tracing out the photonic degrees of freedom (Fig. 3(a)). S_{e1} grows with g

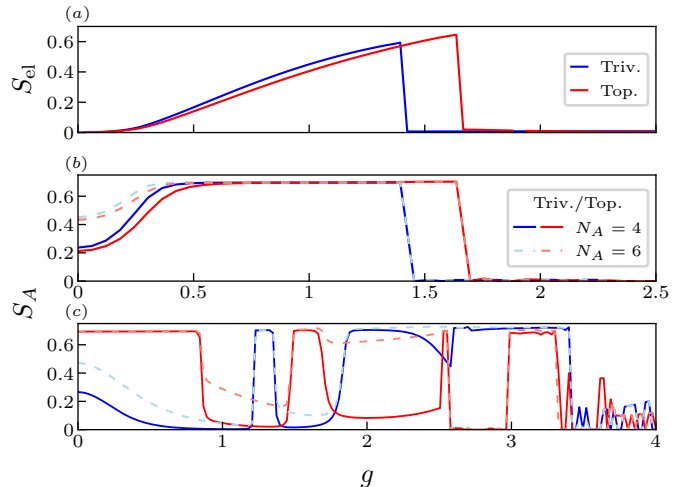


Figure 3: (a) S_{e1} vs g , for the ground state (b) S_A vs g for different partitions N_A and the system in its ground state. (c) S_A for the system in its $N/2$ -th state. Parameters: $\Omega = 10$, $|\delta| = 0.6$, and $N = 20$

and suddenly drops at a critical coupling value, which is different for the trivial and topological phase and reproduces the phase transition captured by the order parameter $\langle Z \rangle$ [17]. The alternative partition requires to first integrate out the photonic degrees of freedom. The resulting density matrix for the fermionic chain encodes the role of photons and can be divided in two parts $A = \{1, 2, \dots, N_A\}$ and $B = \{N_A + 1, N_A + 2, \dots, N\}$ (with $N_A \neq N/2$) of which the entropy can be calculated. From a topological perspective, the entanglement between these partitions has been already studied in non-interacting systems and can differentiate between topological phases [20].

In Fig. 3(b) we plot S_A for the system in its ground state. Its behaviour is very similar to that of S_{e1} and can be used to obtain information about the phase diagram for $\langle Z \rangle$. The saturation to $\log 2$ indicates that the ground state becomes a cat state for finite g , which is destroyed when the system polarizes (i.e., $\langle Z \rangle \neq 0$), turning into a fully localized state.

In contrast, Fig. 3(c) considers the $N/2$ -th state occupied. This state coincides with the edge state in the topological phase and with the top of the valence band in the trivial phase for the isolated chain. The topological phase displays a quantized value $S_A = \log 2$ for small g , independent of the partition, indicating the presence of a maximally entangled state between the boundaries of the system [20]. We can see that the topological boundary mode is present until the entropy drops and the entanglement for the $N/2$ -th state is destroyed, coinciding with

the first anti-crossing of the edge state with a bulk state [17].

The persistence of the $\log(2)$ value for S_A in the topological chain for small g means the interaction preserves the entanglement between ending sites created by the original topological boundary modes, though their energy and localization length does change due to the symmetry breaking. This can have important implications for designing quantum information protocols with c-QED structures in which correlation between distant sites needs to be exploited: in this case, it is naturally provided by the non-trivial topology. The fate of the topological contribution to the entanglement after S_A drops to zero at $g \sim 0.8$ is discussed at [17].

Increasing g leads to a succession of new $\log 2$ plateaus, indicating that boundary modes are linked with both the original trivial and topological phases [21–23]. Again, each abrupt change in S_A coincides with an anti-crossing between the $N/2$ -th and other states in the upper bands [17]. Finally, when g approaches the divergence in Fig. 2 the entropy drops for both phases and the presence of boundary modes is completely washed out.

Conclusions and outlook. – We have investigated the use of the cavity transmission t_c as a topological marker for arbitrary g in a hybrid system, composed of a quantum cavity coupled to a fermionic lattice with distinct topological phases. We consider a topological SSH chain interacting via the dipolar coupling with the cavity, but the framework developed can be applied to the study of other non-trivial topological lattices. We have proven that the measurement of t_c is linked to the topological properties of the unperturbed sample even beyond the small- g regime, when there is a strong hybridization between subsystems. We have considered that the lowest-energy state of the system is occupied, so that the measurement can be performed after the system has thermalized.

The current state-of-the-art techniques would allow to implement our findings with superconducting qubits interacting with microwave photons [24], where g can reach values comparable to the energy of the qubit [25–28]. Additionally, the SSH model has also been realized using superconducting qubits [29]. Quantum dots in c-QED architectures have also verified the crucial condition $g > \{\kappa, \gamma\}$ [30–43], though the values of g that are reached would only allow for topological detection in the small- g regime, occupying an edge state [17]. In this setup, aligning the cavity electric field with the axis of the chain would lead to the dipole interaction, as considered in [44, 45] and implemented in [42, 43] for triple quantum dots.

We believe our work provides a solid basis to study topological systems coupled to quantum cavities, while opening the way to complementary research. Lastly, the employment of the entanglement entropy to study the effect

of the interaction upon the fermionic system sets a precedent in the field, since it is usually used to characterize topology in non-interacting systems.

Acknowledgements

We thank M. Benito and S. Kohler for fruitful discussions. This work was supported by: Ministerio de Economía y Competitividad, through Grant MAT2017- 86717-P (CSIC Research Platform PTI-001) and PID2020-117787GB-I00, Ministerio de Educación y Formación Profesional, under the program FPU, with reference FPU17/05297 (B. P.-G.), the Spanish project PGC2018-094792-B-100 (MCIU/AEI/FEDER, EU) (A. G.-L.).

-
- [1] H. Walther, B. T. H. Varcoe, B.-G. Englert, and T. Becker, Reports on Progress in Physics **69**, 1325 (2006), URL <https://doi.org/10.1088%2F0034-4885%2F69%2F5%2F02>.
 - [2] A. Cottet, M. C. Dartiailh, M. M. Desjardins, T. Cubaynes, L. C. Contamin, M. Delbecq, J. J. Viennot, B. Douçot, and T. Kontos, J. Phys.: Condens. Matter **29** (2017).
 - [3] J. Li and M. Eckstein, Phys. Rev. Lett. **125**, 217402 (2020), URL <https://link.aps.org/doi/10.1103/PhysRevLett.125.217402>.
 - [4] A. Blais, R.-S. Huang, A. Wallraff, S. M. Girvin, and R. J. Schoelkopf, Phys. Rev. A **69**, 062320 (2004), URL <https://link.aps.org/doi/10.1103/PhysRevA.69.062320>.
 - [5] T. Pellizzari, S. A. Gardiner, J. I. Cirac, and P. Zoller, Phys. Rev. Lett. **75**, 3788 (1995).
 - [6] A. Blais, J. Gambetta, A. Wallraff, D. I. Schuster, S. M. Girvin, M. H. Devoret, and R. J. Schoelkopf, Phys. Rev. A **75**, 032329 (2007).
 - [7] D. Matsukevich and A. Kuzmich, Science **306**, 663 (2004).
 - [8] J. I. Cirac, P. Zoller, H. J. Kimble, and H. Mabuchi, Phys. Rev. Lett. **78**, 3221 (1997), URL <https://link.aps.org/doi/10.1103/PhysRevLett.78.3221>.
 - [9] C. A. Downing, T. J. Sturges, G. Weick, M. Stobińska, and L. Martín-Moreno, Phys. Rev. Lett. **123**, 217401 (2019), URL <https://link.aps.org/doi/10.1103/PhysRevLett.123.217401>.
 - [10] W. Nie and Y.-x. Liu, Phys. Rev. Research **2**, 012076 (2020), URL <https://link.aps.org/doi/10.1103/PhysRevResearch.2.012076>.
 - [11] M. C. Dartiailh, T. Kontos, B. Douçot, and A. Cottet, Phys. Rev. Lett. **118**, 126803 (2017), URL <https://link.aps.org/doi/10.1103/PhysRevLett.118.126803>.
 - [12] O. Dmytruk, M. Trif, and P. Simon, Phys. Rev. B **92**, 245432 (2015).
 - [13] B. Pérez-González, M. Bello, A. Gómez-León, and G. Platero, Phys. Rev. B **99**, 035146 (2019), URL <https://link.aps.org/doi/10.1103/PhysRevB.99.035146>.

- [14] B. Pérez-González, M. Bello, G. Platero, and A. Gómez-León, *Phys. Rev. Lett.* **123**, 126401 (2019).
- [15] M. Bello, C. Creffield, and G. Platero, *Scientific Reports* **6** (2016).
- [16] C. Gardiner and P. Zoller, *Quantum Noise: A Handbook of Markovian and Non-Markovian Quantum Stochastic Methods with Applications to Quantum Optics* (Springer-Verlag Berlin Heidelberg, 2004).
- [17] See Supplementary Information for further details on the analytical calculations regarding input-output theory, photonic Green functions, and the effective Hamiltonian, as well as additional numerical results, as the solution for $\langle Z \rangle$, the example of topological detection occupying the edge state, or the connection between the entanglement entropy and the energy spectrum of the system.
- [18] S. Kohler, *Phys. Rev. A* **98**, 023849 (2018), URL <https://link.aps.org/doi/10.1103/PhysRevA.98.023849>.
- [19] A. Cottet, T. Kontos, and B. Douçot, *Phys. Rev. B* **91**, 205417 (2015), URL <https://link.aps.org/doi/10.1103/PhysRevB.91.205417>.
- [20] S. Ryu and Y. Hatsugai, *Phys. Rev. B* **73**, 245115 (2006), URL <https://link.aps.org/doi/10.1103/PhysRevB.73.245115>.
- [21] V. Gurarie, *Phys. Rev. B* **83**, 085426 (2011), URL <https://link.aps.org/doi/10.1103/PhysRevB.83.085426>.
- [22] S. R. Manmana, A. M. Essin, R. M. Noack, and V. Gurarie, *Phys. Rev. B* **86**, 205119 (2012), URL <https://link.aps.org/doi/10.1103/PhysRevB.86.205119>.
- [23] A. Gómez-León, *Phys. Rev. B* **94**, 035144 (2016), URL <https://link.aps.org/doi/10.1103/PhysRevB.94.035144>.
- [24] X. Gu, A. F. Kockum, A. Miranowicz, Y. xi Liu, and F. Nori, *Physics Reports* **718-719**, 1 (2017), ISSN 0370-1573, microwave photonics with superconducting quantum circuits, URL <https://www.sciencedirect.com/science/article/pii/S0370157317303290>.
- [25] A. Baust, E. Hoffmann, M. Haerberlein, M. J. Schwarz, P. Eder, J. Goetz, F. Wulschner, E. Xie, L. Zhong, F. Quijandria, et al., *Phys. Rev. B* **93**, 214501 (2016), URL <https://link.aps.org/doi/10.1103/PhysRevB.93.214501>.
- [26] P. Forn-Díaz, J. Lisenfeld, D. Marcos, J. J. García-Ripoll, E. Solano, C. J. P. M. Harmans, and J. E. Mooij, *Phys. Rev. Lett.* **105**, 237001 (2010), URL <https://link.aps.org/doi/10.1103/PhysRevLett.105.237001>.
- [27] T. Niemczyk, F. Deppe, H. Huebl, E. P. Menzel, F. Hocke, M. J. Schwarz, J. J. Garcia-Ripoll, D. Zueco, T. Hümmer, E. Solano, et al., *Nature Physics* **6**, 772 (2010), ISSN 1745-2481, URL <https://doi.org/10.1038/nphys1730>.
- [28] F. Yoshihara, T. Fuse, S. Ashhab, K. Kakuyanagi, S. Saito, and K. Semba, *Nature Physics* **13**, 44 (2017), ISSN 1745-2481, URL <https://doi.org/10.1038/nphys3906>.
- [29] I. S. Besedin, M. A. Gorlach, N. N. Abramov, I. Tsitsilin, I. N. Moskalenko, A. A. Dobronosova, D. O. Moskalev, A. R. Matanin, N. S. Smirnov, I. A. Rodionov, et al., *Phys. Rev. B* **103**, 224520 (2021), URL <https://link.aps.org/doi/10.1103/PhysRevB.103.224520>.
- [30] A. Stockklauser, P. Scarlino, J. V. Koski, S. Gasparinetti, C. K. Andersen, C. Reichl, W. Wegscheider, T. Ihn, K. Ensslin, and A. Wallraff, *Phys. Rev. X* **7**, 011030 (2017), URL <https://link.aps.org/doi/10.1103/PhysRevX.7.011030>.
- [31] A. Stockklauser, P. Scarlino, J. V. Koski, S. Gasparinetti, C. K. Andersen, C. Reichl, W. Wegscheider, T. Ihn, K. Ensslin, and A. Wallraff, *Phys. Rev. X* **7**, 011030 (2017), URL <https://link.aps.org/doi/10.1103/PhysRevX.7.011030>.
- [32] X. Mi, J. M. Cady, D. M. Zajac, P. W. Deelman, and J. R. Petta, *Science* **355** (2017).
- [33] L. E. Bruhat, T. Cubaynes, J. J. Viennot, M. C. Dartiailh, M. M. Desjardins, A. Cottet, and T. Kontos, *Phys. Rev. B* **98**, 155313 (2018), URL <https://link.aps.org/doi/10.1103/PhysRevB.98.155313>.
- [34] D. J. van Woerkom, P. Scarlino, J. H. Ungerer, C. Müller, J. V. Koski, A. J. Landig, C. Reichl, W. Wegscheider, T. Ihn, K. Ensslin, et al., *Phys. Rev. X* **8**, 041018 (2018), URL <https://link.aps.org/doi/10.1103/PhysRevX.8.041018>.
- [35] B. Wang, T. Lin, H. Li, S. Gu, M. Chen, G. Guo, H. Jiang, X. Hu, G. Cao, and G. Guo, *Science Bulletin* **66**, 332 (2021), ISSN 2095-9273, URL <https://www.sciencedirect.com/science/article/pii/S2095927320306587>.
- [36] D. Najer, I. Söller, P. Sekatski, V. Dolique, M. C. Löbl, D. Riedel, R. Schott, S. Starosielec, S. R. Valentin, A. Wieck, et al., *Nature* **5**, 622 (2019).
- [37] N. Samkharadze, G. Zheng, N. Kalhor, D. Brousse, A. Sammak, U. C. Mendes, A. Blais, G. Scappucci, and L. M. K. Vandersypen, *Science* **359** (2018).
- [38] X. Mi, M. Benito, S. Putz, D. M. Zajac, J. M. Taylor, G. Burkard, and J. R. Petta, *Nature* **555**, 590 (2018).
- [39] T. Cubaynes, M. R. Delbecq, M. C. Dartiailh, R. Assouly, M. M. Desjardins, L. C. Contamin, L. E. Bruhat, Z. Leghtas, F. Mallet, A. Cottet, et al., *npj Quantum Information* **5** (2019).
- [40] X. G. Borjans, F. Croot, X. Mi, M. J. Gullans, and J. R. Petta, *Nature* **577**, 195 (2020).
- [41] N. Samkharadze, G. Zheng, N. Kalhor, D. Brousse, A. Sammak, U. C. Mendes, A. Blais, G. Scappucci, and L. M. K. Vandersypen, *Science* **359**, 1123 (2018).
- [42] A. J. Landig, J. V. Koski, P. Scalino, U. C. Mendes, A. Blais, C. Reichl, W. Wegscheider, A. Wallraff, K. Ensslin, and T. Ihn, *Nature* **560**, 179 (2018).
- [43] A. J. Landig, J. V. Koski, P. Scarlino, C. Müller, J. C. Abadillo-Uriel, B. Kratochwil, C. Reichl, W. Wegscheider, S. N. Coppersmith, M. Friesen, et al., *Nature Communications* **10** (2019).
- [44] M. Russ, F. Ginzel, and G. Burkard, *Phys. Rev. B* **94**, 165411 (2016), URL <https://link.aps.org/doi/10.1103/PhysRevB.94.165411>.
- [45] V. Srinivasa, J. M. Taylor, and C. Tahan, *Phys. Rev. B* **94**, 205421 (2016), URL <https://link.aps.org/doi/10.1103/PhysRevB.94.205421>.
- [46] D. F. Walls and G. J. Milburn, *Quantum Optics* (Springer, 2008).

Appendix A: Input-output formalism

Using the initial Hamiltonian

Consider the initial Hamiltonian describing a transmission line with two ports, coupled to the topological system via the cavity photons. The total Hamiltonian is:

$$H = \Omega d^\dagger d + H_S + g (d^\dagger + d) Z + H_B, \quad (\text{A1})$$

with H_B being the Hamiltonian for the electromagnetic field in the transmission line and its coupling to the cavity,

$$\begin{aligned} H_B = & \sum_{l=1,2} \int_{-\infty}^{\infty} \omega b_l^\dagger(\omega) b_l(\omega) d\omega \\ & + i \sum_{l=1,2} \int_{-\infty}^{\infty} \left[\mu_l(\omega) b_l^\dagger(\omega) d \right. \\ & \left. - \mu_l(\omega)^* d^\dagger b_l(\omega) \right] d\omega \end{aligned} \quad (\text{A2})$$

where $l = 1, 2$ represent the left/right sides of the cavity, $b_l(\omega)$ is the destruction operator for a photon with energy ω at side l of the cavity and $\mu_l(\omega)$ represents the coupling between the cavity and the outside modes. In this work, we will consider the Markov approximation, which gives $\mu_l(\omega) = \sqrt{\kappa_l/2\pi}$.

Then, the first step is to derive the equation of motion (EoM) for the transmission line photons:

$$\frac{d}{dt} b_l(\nu, t) = -i\nu b_l(\nu, t) + \sqrt{\frac{\kappa_l}{2\pi}} d(t) \quad (\text{A3})$$

which can be formally integrated to yield

$$\begin{aligned} b_l(\nu, t) = & b_l(\nu, t_0) e^{-i\nu(t-t_0)} \\ & + \sqrt{\frac{\kappa_l}{2\pi}} \int_{t_0}^t dt' e^{-i\nu(t-t')} d(t') \end{aligned} \quad (\text{A4})$$

where $t_0 < t$ represents the initial condition. Inserting the previous expression into the EoM for the cavity photons, we get

$$\begin{aligned} \frac{d}{dt} d(t) = & -i\Omega d(t) - igZ(t) - \sum_{l=1,2} \sqrt{\frac{\kappa_l}{2\pi}} \int_{-\infty}^{\infty} d\nu b_l(\nu, t) \\ = & -i \left(\Omega - i\frac{\kappa}{2} \right) d(t) - igZ(t) \\ & - \sum_{l=1,2} \sqrt{\kappa_l} b_{in,l}(t) \end{aligned} \quad (\text{A5})$$

where $\kappa = \kappa_1 + \kappa_2$, and we have defined an input field,

$$b_{in,l}(t) = \frac{1}{\sqrt{2\pi}} \int_{-\infty}^{\infty} b_l(\nu, t_0) e^{-i\nu(t-t_0)} d\nu. \quad (\text{A6})$$

Similarly, the solution for $b_l(\nu, t)$ in (A4) can also be obtained in terms of a final condition $t_1 > t$, which let us define an output field $b_{out,l}(t)$, fulfilling

$$b_{out,l}(t) = b_{in,l}(t) + \sqrt{\kappa_l} d(t) \quad (\text{A7})$$

One has to solve the EoM for $Z(t)$ as well. We consider the basis of eigenstates of the fermionic Hamiltonian

$$H_S = \sum_{\alpha=1}^N E_\alpha X^{\alpha,\alpha}, \quad Z = \sum_{\bar{\alpha}} Z_{\bar{\alpha}} X^{\bar{\alpha}} \quad (\text{A8})$$

with $X^{\bar{\alpha}} = X^{\alpha_1, \alpha_2} = |\alpha_1\rangle\langle\alpha_2|$, and calculate the equation of motion for an arbitrary Hubbard operator $X^{\bar{\alpha}}$

$$\begin{aligned} \partial_t \tilde{X}^{\bar{\alpha}}(t) = & i \left(\tilde{E}_{\bar{\alpha}} - i\frac{\gamma}{2} \right) \tilde{X}^{\bar{\alpha}}(t) \\ & + ig (d^\dagger(t) + d(t)) \sum_{\beta} \left(\tilde{Z}_{\beta, \alpha_1} \tilde{X}^{\beta, \alpha_2}(t) \right. \\ & \left. - \tilde{Z}_{\alpha_2, \beta} \tilde{X}^{\alpha_1, \beta}(t) \right), \end{aligned} \quad (\text{A9})$$

where $E_{\bar{\alpha}} = E_{\alpha_1} - E_{\alpha_2}$ and we have also included the phenomenological spectral broadening factor $\gamma/2$. The product $d^{(\dagger)}(t) X(t)$ can be decomposed as

$$d^{(\dagger)}(t) X(t) \approx \langle X \rangle d^{(\dagger)}(t) + \langle d^{(\dagger)} \rangle X(t), \quad (\text{A10})$$

where we are neglecting any terms accounting for correlation between operators, which is a valid approach in the small- g regime. Under this condition, one can safely calculate $\langle X \rangle$ and $\langle d^{(\dagger)} \rangle$ using the corresponding unperturbed Hamiltonians, H_S and $\Omega d^\dagger d$, respectively. Then, one can easily see that $\langle d^{(\dagger)} \rangle = 0$, and hence the solution for the EoM in (A9) in frequency space reads

$$X^{\bar{\alpha}}(\omega) \simeq gd(\omega) \frac{\sum_{\beta} (Z_{\alpha_2, \beta} \langle X^{\alpha_1, \beta} \rangle - Z_{\beta, \alpha_1} \langle X^{\beta, \alpha_2} \rangle)}{\omega + E_{\bar{\alpha}} - i\frac{\gamma}{2}}. \quad (\text{A11})$$

We have also neglected the contribution of $\langle X \rangle d^\dagger(\omega)$, as typically done in the literature [18]. Substituting this result in (A5), we find

$$d(\omega) = \frac{i \sum_{l=1,2} \sqrt{\kappa_l} b_{in,l}(\omega)}{\Omega - \omega - i\frac{\kappa}{2} + g^2 \chi(\omega)} \quad (\text{A12})$$

where

$$\chi(\omega) = \sum_{\bar{\alpha}, \beta} \frac{Z_{\bar{\alpha}} (Z_{\alpha_2, \beta} \langle X^{\alpha_1, \beta} \rangle - Z_{\beta, \alpha_1} \langle X^{\beta, \alpha_2} \rangle)}{\omega + E_{\bar{\alpha}} - i\frac{\gamma}{2}}. \quad (\text{A13})$$

Using (A7), and taking into account that the input is inserted through the left port ($l = 1$) into the cavity, and the output is collected through the right one ($l = 2$), we can write the transmission as

$$t_c(\omega) = \frac{\langle b_{\text{out}, 2} \rangle}{\langle b_{\text{in}, 1} \rangle} = \frac{i\sqrt{\kappa_1 \kappa_2}}{\Omega - \omega - i\frac{\kappa}{2} + g^2 \chi(\omega)} \quad (\text{A14})$$

which is the usual result for the cavity transmission, with $\chi(\omega)$ being the electronic susceptibility.

Using the mean-field Hamiltonian

If we instead consider the MF Hamiltonian for the cavity, topological system and their interaction, we start from the following expression

$$\begin{aligned} H = & \Omega d^\dagger d - \frac{g^2 \langle Z \rangle^2}{\Omega} + \tilde{H}_S + g(d^\dagger + d) \tilde{Z} \\ & + \sum_{l=1,2} \int_{-\infty}^{\infty} \omega b_l^\dagger(\omega) b_l(\omega) d\omega \\ & + i \sum_{l=1,2} \sqrt{\frac{\gamma_l}{2\pi}} \int_{-\infty}^{\infty} d\omega \left[b_l^\dagger(\omega) \left(d - \frac{g \langle Z_l \rangle}{\Omega} \right) \right. \\ & \quad \left. - \left(d^\dagger - \frac{g \langle Z_l \rangle}{\Omega} \right) b_l(\omega) \right] \end{aligned} \quad (\text{A15})$$

where $\tilde{Z} = Z - \langle Z \rangle$ and $\tilde{H}_S = H_S - \frac{2g^2 \langle Z \rangle}{\Omega} Z$. Note that the cavity operators have been rotated to $\tilde{d}^{(\dagger)} = d^{(\dagger)} - \frac{g \langle Z \rangle}{\Omega}$ in order to diagonalize their MF Hamiltonian. The self-consistent values of $\langle Z \rangle$ and $\langle d^{(\dagger)} \rangle$ have been determined ignoring the coupling to the transmission line, as explained in the main text. Importantly, the cavity operators in H_B have also been rotated accordingly. This time, the EoM for $b_l(\nu, t)$ yields the following solution

$$\tilde{b}_l(\nu, t) = b_l(\nu, t) - \frac{g \langle Z_l \rangle}{\Omega} \sqrt{\frac{\kappa_l}{2\pi}} \frac{1 - e^{-i\nu(t-t_0)}}{i\nu} \quad (\text{A16})$$

Compared to (A4), we have an extra term due to the rotation of the bosonic operators, that depends on the state of the fermionic system through $\langle Z \rangle$. The EoM for $d(t)$ has the same form, with redefined input and output fields

$$\tilde{b}_{\text{in}, l}(t) = b_{\text{in}, l}(t) - \frac{g\sqrt{\kappa_l} \langle Z_l \rangle}{2\pi\Omega} \int_{-\infty}^{\infty} \frac{1 - e^{-i\nu(t-t_0)}}{i\nu} d\nu, \quad (\text{A17})$$

$$\tilde{b}_{\text{out}, l}(t) = b_{\text{out}, l}(t) + \frac{g\sqrt{\kappa_l} \langle Z_l \rangle}{2\pi\Omega} \int_{-\infty}^{\infty} \frac{1 - e^{i\nu(t_1-t)}}{i\nu} d\nu, \quad (\text{A18})$$

also fulfilling that $\tilde{b}_{\text{out}, l}(t) = \tilde{b}_{\text{in}, l}(t) + \sqrt{\kappa_l} d(t)$. On the other hand, the Hubbard operators change as well due to the presence of the extra MF contribution in the fermionic Hamiltonian

$$\tilde{H}_S = H_S - \frac{2g^2 \langle Z \rangle}{\Omega} Z = \sum_{\alpha=1}^N \tilde{E}_\alpha \tilde{X}^{\alpha, \alpha}, \quad (\text{A19})$$

$$\tilde{Z} = \sum_{\bar{\alpha}} \tilde{Z}_{\bar{\alpha}} \tilde{X}^{\bar{\alpha}}. \quad (\text{A20})$$

The EoM for \tilde{X} has the same form of (A9), but substituting the eigenvalues and eigenvectors of the unperturbed fermionic Hamiltonian H_S by the ones of MF Hamiltonian \tilde{H}_S . To solve the EoM, we take fluctuations to be small, which is a valid assumption when g is both small and very large, i.e., when the MF Hamiltonian $\tilde{H}_S + \tilde{H}_\Omega$ accurately describes the physics of the system, without considering the fluctuations Hamiltonian \tilde{H}_δ . Under this condition, we can write $d^{(\dagger)}(t) \tilde{X}(t) \approx \langle \tilde{X} \rangle d^{(\dagger)}(t) + \langle d^{(\dagger)} \rangle \tilde{X}(t)$. Again, we neglect any correlation created by the fluctuations Hamiltonian, which acts as an effective interaction between the two MF Hamiltonians. Note that $\langle d^{(\dagger)} \rangle = 0$ when evaluated using the MF photonic Hamiltonian in the rotated frame, \tilde{H}_Ω . Formally, the decoupling employed to solve (A20) is the same as the one used in (A9). Then, the solution for \tilde{X} gives

$$\tilde{X}^{\bar{\alpha}}(\omega) \simeq g d(\omega) \frac{\sum_{\beta} \left(\tilde{Z}_{\alpha_2, \beta} \langle \tilde{X}^{\alpha_1, \beta} \rangle - \tilde{Z}_{\beta, \alpha_1} \langle \tilde{X}^{\beta, \alpha_2} \rangle \right)}{\omega + \tilde{E}_{\bar{\alpha}} - i\frac{\gamma}{2}}. \quad (\text{A21})$$

Note that (A13) is analogous to (A21), but all parameters have been renormalized due to MF. Finally, the transmission can be written as

$$t_c(\omega) = \frac{i\sqrt{\kappa_1 \kappa_2}}{\Omega - \omega - i\frac{\kappa}{2} + g^2 \tilde{\chi}(\omega)}. \quad (\text{A22})$$

where now $\tilde{\chi}(\omega)$ is the susceptibility written in terms of the MF Hamiltonian.

Appendix B: Transmission and photonic Green's function

The starting point is the EoM for the photonic operator $d(t)$ (A5) in Fourier space

$$i\omega d(\omega) = -i\left(\Omega - i\frac{\kappa}{2}\right)d(\omega) - ig\sum_{\tilde{\alpha}} Z_{\tilde{\alpha}}\tilde{X}^{\tilde{\alpha}}(\omega) - \sum_{l=1,2}\sqrt{\kappa_l}\tilde{b}_{\text{in},l}(\omega) \quad (\text{B1})$$

The losses of the cavity have been included through the phenomenological factor κ . This equation depends on $\tilde{X}^{\tilde{\alpha}}(\omega)$, which has its own dynamics as well,

$$i\omega\tilde{X}^{ij}(\omega) = -i\left(\tilde{E}_j - \tilde{E}_i + i\frac{\gamma}{2}\right)\tilde{X}^{ij}(\omega) - ig(d^\dagger(\omega) + d(\omega))\sum_m\left(Z_{jm}\tilde{X}^{im}(\omega) - Z_{mi}\tilde{X}^{mj}(\omega)\right). \quad (\text{B2})$$

Solving this equation implies writing the EoM for $d^{(\dagger)}\tilde{X}^{ij}$, which at the same time is coupled to higher-order operators. Then, we can write an infinite vector with all the relevant operators involved, $\vec{v} = (d, X^{ij}, \dots)$, and the system of equations turns out to be

$$(\omega - A)\vec{v} = \vec{v}_0 \quad (\text{B3})$$

where A is the coefficients matrix and \vec{v}_0 represents the inhomogeneous term.

Then, on the other hand, we can write the EoM for the retarded photonic Green function, defined as $G(t) = -i\theta(t)\langle[d(t), d^\dagger]\rangle \equiv \langle\langle d(t); d^\dagger \rangle\rangle_t$, yielding

$$\omega G(\omega) = 1 + \left(\Omega - i\frac{\kappa}{2}\right)\tilde{G}(\omega) + g\sum_{ij}M_{ij}(\omega) \quad (\text{B4})$$

where $\tilde{M}_{ij}(\omega) = \langle\langle X^{ij}; a^\dagger \rangle\rangle_\omega$. Note that the dissipative factor enters the EoM for $G(\omega)$ through the integration of the external modes and their coupling to the cavity photons, just as in Eq. A5. Again, this EoM is coupled to higher-order Green functions, resulting in an infinite system of coupled differential equations. In matrix form, we have

$$(\omega - A')\vec{V}(\omega) = \vec{V}_0 \quad (\text{B5})$$

where $\vec{V} = (G, M_{ij}, \dots)$ and \vec{V}_0 is the inhomogeneous term by comparison. One can see that $A = A'$, which indicates that $G(\omega) = -i\theta(t)\langle[a(t), a^\dagger]\rangle$ is the resolvent of (B1).

Finally, we can compare the first component of each system of equations, namely $a(\omega) = -i(\omega - H)^{-1}\sum_{l=1,2}\sqrt{\kappa_l}\tilde{b}_{\text{in},l}(\omega)$ and $G(\omega) = (\omega - H)^{-1}$, and see that

$$a(\omega) = -iG(\omega)\sum_{l=1,2}\sqrt{\kappa_l}\tilde{b}_{\text{in},l}(\omega). \quad (\text{B6})$$

The last step is to write the transmission as a function of $a(\omega)$, knowing that $\tilde{b}_{\text{out},l}(t) = \tilde{b}_{\text{in},l}(\omega) + \sqrt{\kappa_l}a(\omega)$ and that the only input is through port 1

$$t_c = \frac{\langle\tilde{b}_{\text{out},2}\rangle}{\langle\tilde{b}_{\text{in},1}\rangle} = \frac{\langle\tilde{b}_{\text{in},2}\rangle + \sqrt{\kappa_2}\langle a \rangle}{\langle\tilde{b}_{\text{in},1}\rangle} = -i\sqrt{\kappa_2}\sqrt{\kappa_1}G(\omega). \quad (\text{B7})$$

It is very enlightening to obtain an analytical expression for the photonic Green function in the case of $g \ll \Omega, \tilde{E}_{\tilde{\alpha}}$ and $g \gg \Omega, \tilde{E}_{\tilde{\alpha}}$. The equation of motion of $G(\omega)$ (Eq. B4) is coupled to the mixed Green function \tilde{M}_{ij} , which gives

$$\omega\tilde{M}_{ij} = (\tilde{E}_j - \tilde{E}_i)\tilde{M}_{ij} + \sum_l Z_{jl}\langle\langle(d^\dagger + d)\tilde{X}^{il}; d^\dagger\rangle\rangle_\omega - \sum_l Z_{li}\langle\langle(d^\dagger + d)\tilde{X}^{lj}; d^\dagger\rangle\rangle \quad (\text{B8})$$

Note the presence of the higher-order Green function $\langle\langle(d^\dagger + d)\tilde{X}; d^\dagger\rangle\rangle$. Fluctuations are negligible in the small and very-large coupling regimes, which let us employ the following decoupling scheme

$$\langle\langle(d^\dagger + d)\tilde{X}; d^\dagger\rangle\rangle \approx (\langle d^\dagger \rangle + \langle d \rangle)\langle\langle\tilde{X}; d^\dagger\rangle\rangle_\omega + \langle\tilde{X}\rangle\langle\langle d; d^\dagger \rangle\rangle_\omega \quad (\text{B9})$$

This approximation is analogous to the decoupling scheme $d^{(\dagger)}(t)\tilde{X}(t) \approx \langle\tilde{X}\rangle d^{(\dagger)}(t) + \langle d^{(\dagger)} \rangle \tilde{X}(t)$ presented in the main text used to solve the EoM for the photonic operator. Again, it implies that we are neglecting first-order correlations between fermionic and photonic operators, and under this assumption the system of equations including Eqs. B4 and B8 can be closed and solved, obtaining

$$G(\omega) = -\frac{1}{\Omega - \omega + g^2\tilde{\chi}(\omega)}. \quad (\text{B10})$$

for the photonic Green function. It is straight-forward to see that the previous expression verifies the relation between the transmission and $G(\omega)$ presented in Eq. 5, when compared with Eq. 7 in the limits of $g \ll \Omega$, $\tilde{E}_{\tilde{\alpha}}$ and $g \gg \Omega$, $\tilde{E}_{\tilde{\alpha}}$.

Appendix C: Solution for $\langle Z \rangle$

In order to solve the self-consistency equation for the order parameter $\langle Z \rangle = \sum_{\tilde{\alpha}} \tilde{Z}_{\tilde{\alpha}} \langle \tilde{X}^{\tilde{\alpha}} \rangle$, we iterate until convergence using the eigenstates of the MF Hamiltonian \tilde{H}_S in Eq. 2, and also those of the total Hamiltonian $\tilde{H}_{\delta} + \tilde{H}_S + \tilde{H}_{\Omega}$ to compare with the exact value.

Fig. 4 shows $\langle Z \rangle$ as a function of g for the MF case and the exact one, and provides us a precise value for the breakdown of the approximation. Different chain lengths N have also been considered. As expected, the MF calculation agrees with the exact value at small and large g . In the former case, $\langle Z \rangle = 0$ indicates that the MF Hamiltonian coincides with the free Hamiltonian, and that the symmetries of the model are unaffected by the coupling with the cavity. In the latter, the system polarizes (i.e., $\langle Z \rangle \neq 0$) indicating that the ground state of the system is modified and that certain symmetries change. For intermediate values, fluctuations take over and lead to disagreement between the MF and the exact solution. The MF result indicates that the change in $\langle Z \rangle$ is continuous, corresponding to a second-order phase transition. However, the exact calculation shows a discontinuity at a critical value for g , which could indicate that is in fact a first order transition.

Interestingly, we find that beyond the critical g a difference between the topological and the trivial phase arises, which is also captured by the MF solution. This is a consequence of the different coupling between bulk/edge modes and the cavity photons. It also indicates that certain features of the topological edge states still remain when the coupling strength is increased beyond the small g regime, but they disappear again at very large g .

$\langle Z \rangle$ also depends on the chain length N . This is intuitive due to the position-dependent interaction: the chain size modifies the value of the critical point at which the system polarizes, enhancing or reducing the difference between topological phases at the phase transition, as well as the final value in the limit $g \rightarrow \infty$. Also, as the number of sites N increases, the critical value of g at which the phase transition happens is reduced (see Fig. 4). This is expected, since the effective strength of the coupling at each site $g_i = gx_i$ gets larger as more sites are considered.

The system size also shapes the differences between topo-

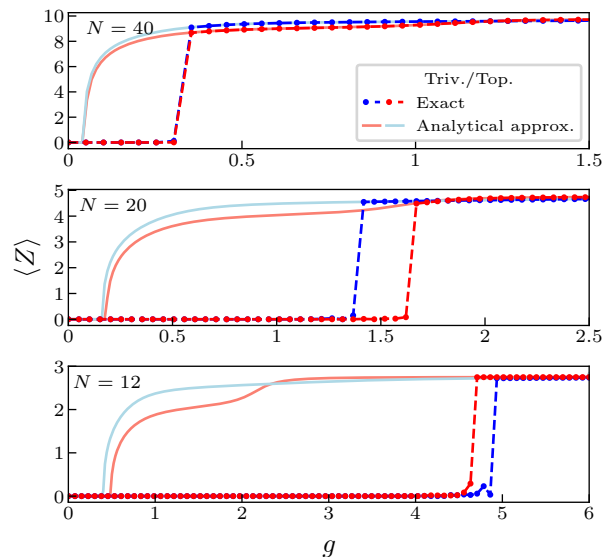


Figure 4: $\langle Z \rangle$ for different N . $\langle Z \rangle$ as a function of the coupling constant g for $\Omega = 10$, $\delta = \pm 0.6$ (trivial/topological phase) and different system sizes: $N = 40$ (top), $N = 20$ (middle), $N = 12$ (bottom). The value of $\langle Z \rangle$ has been calculated self-consistently using the MF Hamiltonian (solid) and exact diagonalization (dashed-dotted line). The chain size modifies the value of the critical point at which the system polarizes, enhancing or reducing the difference between topological phases at the phase transition

logical phases found immediately after the phase transition, that are captured by the MF calculation, without including fluctuations.

Appendix D: Topological detection in the small coupling regime occupying an edge state

We have shown that the cavity transmission cannot act as a topological marker if the lowest-energy state is occupied. On the contrary, if the edge state is initially occupied in the topological phase, the transmission peak at $\omega = \Omega$ should remain unaffected by the interaction, as opposed to the behaviour of the trivial phase, in which changes in t_c are expected. This asymmetry between phases can be maximized if the cavity frequency Ω is resonant with an electronic transition $E_{\tilde{\alpha}}$ (eigenenergy of the unperturbed fermionic Hamiltonian H_S) and in particular, with the gap of the chain. While the transmission for the non-trivial topological phase does not change compared to the uncoupled cavity transmission (the bulk states are decoupled from the edge states), the presence of a direct resonance in the trivial phase results in a Rabi splitting: the peak of maximum transmission divides into two distinct modes, separated by the Rabi frequency Ω_r [46], which is often detected in experiments and indicates that the regime $g > \{\kappa, \gamma\}$ is achieved [30, 32, 38, 41, 42].

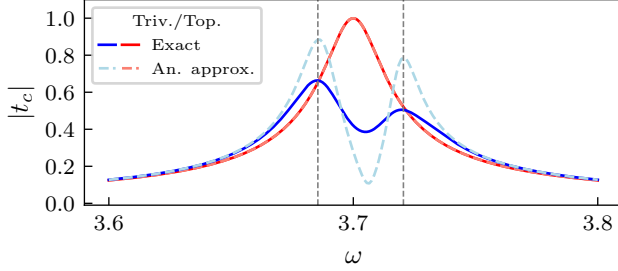


Figure 5: $|t_c(\omega)|$ as a function of ω . Dashed lines indicate the analytical approximation (Eq. 7), while solid lines correspond to the exact solution (Eq. 5). We consider the $(N/2)$ -th state occupied, corresponding to the edge state in the topological phase and the top of the valence band in the trivial phase. The parameters used are: $\Omega = 3.7$, $g = 0.06$, $\delta = \pm 0.925$ (trivial/topological phase, in blue/red, respectively), $N = 20$, $\gamma = \kappa_1 = \kappa_2 = 0.01$.

This is shown in Fig. 5. We consider the top state in the valence band is occupied for the trivial phase, while the edge state is occupied for the topological phase. This choice is motivated by the fact that both states are adiabatically connected across the topological phase transition, as δ is varied from negative to positive values. While the decoupling between bulk and edge states explains the absence of any changes in t_c for the topological phase, a Rabi splitting appears for the trivial phase. The analytical approximation captures the position of each peak in ω (as indicated by the dashed, grey vertical lines), as well as their relative height, though the exact shape of the peaks is not reproduced. This disagreement can be explained by correlated excitations that strongly modify the system due to resonant conditions.

In conclusion, for the small- g regime it is important to stress that detection of the topological phase requires the system to be initialized in an edge state. Otherwise the cavity transmission cannot differentiate between the two phases. One disadvantage of this regime of operation is that the measurement needs to be carried out before thermalization happens, but this could be avoided by filling the fermionic system to half-filling (however, in this case many systems require to account for particle interactions as well).

Appendix E: Schrieffer-Wolff transformation

We begin with the Hamiltonian $H = \tilde{H}_S + \tilde{H}_\Omega + \tilde{H}_\delta$, as defined in the main text, written in the basis of eigenstates of \tilde{H}_S :

$$H = \sum_i \tilde{E}_\alpha \tilde{X}^{\alpha,\alpha} + \Omega d^\dagger d - \frac{g^2 \langle Z \rangle}{\Omega} + g(d^\dagger + d)\tilde{Z} \quad (\text{E1})$$

We propose the following ansatz for the generator S of the Schrieffer-Wolff (S-W) transformation,

$$S = \sum_{\vec{\alpha}} (\Gamma_{\vec{\alpha}}^+ d^\dagger + \Gamma_{\vec{\alpha}}^- d) \tilde{X}^{\vec{\alpha}} \quad (\text{E2})$$

where $\vec{\alpha} = (\alpha_1, \alpha_2)$. Imposing $\tilde{H}_\delta = -[S, \tilde{H}_S + \tilde{H}_\Omega]$, one finds the following equations for the free parameters:

$$\Gamma_{\vec{\alpha}}^\pm = \frac{g \tilde{Z}_{\vec{\alpha}}}{\tilde{E}_{\vec{\alpha}} \pm \Omega}. \quad (\text{E3})$$

with $\tilde{E}_{\vec{\alpha}} = \tilde{E}_{\alpha_1} - \tilde{E}_{\alpha_2}$. This results in the final form of the transformation:

$$S = g(d^\dagger + d) \sum_{\vec{\alpha}} \frac{\tilde{E}_{\vec{\alpha}} \tilde{Z}_{\vec{\alpha}}}{\tilde{E}_{\vec{\alpha}}^2 - \Omega^2} - g\Omega(d^\dagger - d) \sum_{ij} \frac{\tilde{Z}_{\vec{\alpha}}}{\tilde{E}_{\vec{\alpha}}^2 - \Omega^2} \tilde{X}^{\vec{\alpha}} \quad (\text{E4})$$

The correction to the Hamiltonian is proportional to:

$$\begin{aligned} [S, \tilde{H}_\delta] &= g^2(d^\dagger + d)^2 \sum_{\vec{\alpha}} \frac{\tilde{E}_{\vec{\alpha}} \tilde{Z}_{\vec{\alpha}}}{\tilde{E}_{\vec{\alpha}}^2 - \Omega^2} Y_{\vec{\alpha}}^- \\ &\quad - g^2 \Omega (d^{\dagger 2} - d^2) \sum_{\vec{\alpha}} \frac{\tilde{Z}_{\vec{\alpha}}}{\tilde{E}_{\vec{\alpha}}^2 - \Omega^2} Y_{\vec{\alpha}}^- \\ &\quad + g^2 \Omega \sum_{\vec{\alpha}} \frac{\tilde{Z}_{\vec{\alpha}}}{\tilde{E}_{\vec{\alpha}}^2 - \Omega^2} Y_{\vec{\alpha}}^+ \end{aligned} \quad (\text{E5})$$

with

$$Y_{\vec{\alpha}}^\pm = \sum_{\beta} (\tilde{Z}_{\alpha_2 \beta} \tilde{X}^{\alpha_1 \beta} \pm \tilde{Z}_{\beta \alpha_1} X^{\beta \alpha_2}) \quad (\text{E6})$$

Finally, one can write the effective Hamiltonian up to second order, neglecting two-photon processes and constant terms,

$$\begin{aligned} \bar{H} &\simeq \tilde{H}_S + \Omega d^\dagger d + \frac{1}{2} [S, \tilde{H}_\delta] \\ &= \sum_{\alpha} \tilde{E}_{\alpha} \tilde{X}^{\alpha,\alpha} \\ &\quad + \frac{g^2}{2} \sum_{\vec{\alpha}} \tilde{Z}_{\vec{\alpha}} \left[\frac{\sum_{\beta} \tilde{Z}_{\alpha_2 \beta} \tilde{X}^{\alpha_1 \beta}}{\tilde{E}_{\vec{\alpha}} - \Omega} - \frac{\sum_n \tilde{Z}_{\beta \alpha_1} \tilde{X}^{\beta \alpha_2}}{\tilde{E}_{\vec{\alpha}} + \Omega} \right] \\ &\quad + \left[\Omega + g^2 \sum_{\vec{\alpha}} \tilde{\Omega}_{\vec{\alpha}} \tilde{Y}_{\vec{\alpha}}^- \right] d^\dagger d. \end{aligned} \quad (\text{E7})$$

where $\tilde{\Omega}_\alpha$ is defined in the main text.

Appendix F: Entanglement Entropy and Energy Spectrum

As shown in Fig. 3(c) in the main text, there is a $\log(2)$ -plateau in the topological phase for small- g when the $N/2$ -th state is occupied, corresponding to one of the topological edge states. Its drop at $g \sim 0.84$ corresponds with its anti-crossing with a state belonging to the bulk bands and indicates the destruction of maximal entanglement for the $N/2$ -th state.

However, the topological contribution to the entanglement entropy is not lost at this point, but migrates from one state to the other as they further anti-cross in the energy spectrum. Figure 6 shows a zoom of the energy

spectrum where the edge states penetrate into the bulk bands, together with the entanglement entropy S_A associated to the occupation of each of them. For small- g , the $\log(2)$ plateau corresponds to the $N/2$ -th (red) and $(N/2 + 1)$ -th (light brown) states (edge states), while the rest of them are not maximally entangled (their S_A depends on the partition used). The first anti-crossing encountered in the spectrum (at $g \sim 0.78$) between the light brown and blue (top state in the valence band) states, corresponds to the appearance of a $\log(2)$ -plateau for the later, while the entanglement between the ending sites is lost for the edge state.

On the other hand, as g is increased, the $N/2$ -th state anti-crosses with other states as well. Figure 7 shows that each of these anti-crossings correspond to the abrupt changes in S_A obtained for the $N/2$ -th state (Fig. 3(c)), by zooming into the first four of them.

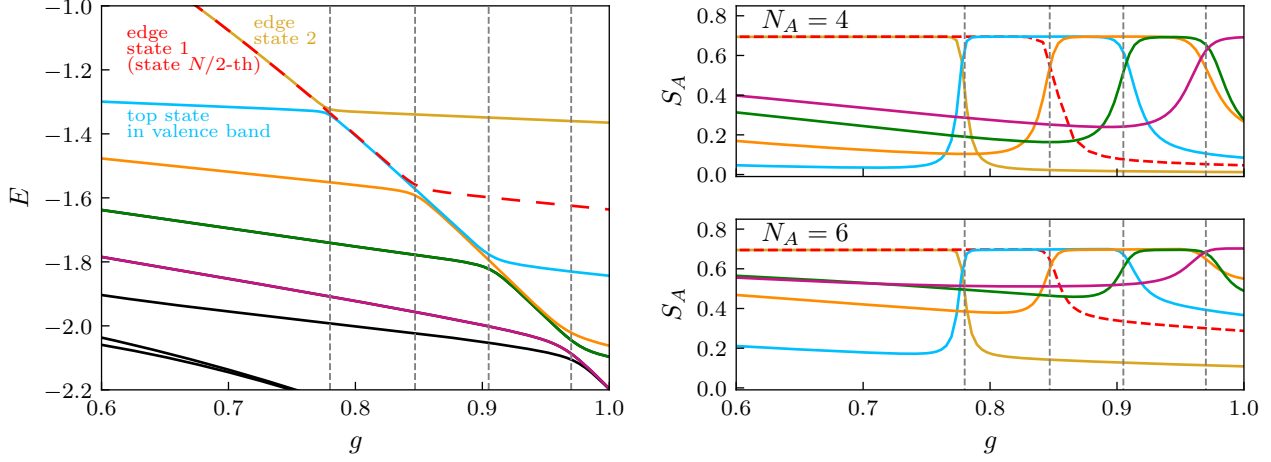


Figure 6: **Entanglement entropy and the energy spectrum.** Left plot: zoom into the energy spectrum, as a function of g , corresponding to the anti-crossing (dashed, grey vertical lines) of energy states triggered by the entrance of the edge states into the bulk band. The parameters chosen are: $\Omega = 10$ $\delta = -0.6$, $N = 20$. Each state is depicted in a different color: light brown for the $(\frac{N}{2} + 1)$ -th state, red for the $N/2$ -th (corresponding to the two edge states), blue for the $(\frac{N}{2} - 1)$ -th (top state in the valence band), orange for the $(\frac{N}{2} - 2)$ -th, green for the $(\frac{N}{2} - 3)$ -th and violet for the $(\frac{N}{2} - 4)$ -th (the following states appear in black). The first anti-crossing at $g \sim 0.78$ happens between the edge state (light brown) and the top state in the valence band (blue). The second anti-crossing at $g \sim 0.9$ happens between the edge state (red) and $(\frac{N}{2} - 2)$ -th state in the bulk band (orange). For higher values of the coupling constant (only shown up to $g = 1$), successive anti-crossings between adjacent states appear. Right plot: entanglement entropy for each state (same color code as in the left plot), for different partitions $N = 4$ (upper plot) and $N = 6$ (lower plot). For small- g , the $\log(2)$ plateau corresponds to the $N/2$ -th state, while the rest of them are not maximally entangled (their S_A depends on the partition used). Each time a state from the bulk band anti-crosses with an edge state, it turns into an edge state itself, so that the $\log(2)$ plateau (originally caused by the non-trivial topology of the fermionic system) migrates from one state to the other.

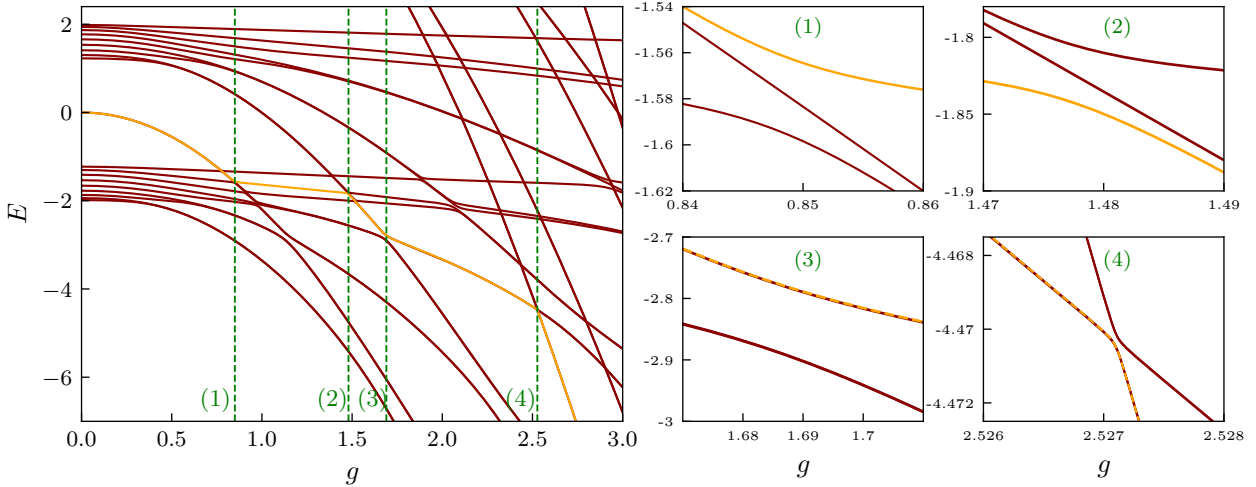


Figure 7: **Anti-crossings for the $N/2^{\text{th}}$ state in the topological phase.** Left plot: energy spectrum for the zero-photon band as a function of g . The $N/2$ -th state (for which the entanglement entropy is calculated in Fig. 6(c)) is represented in orange. The green, dashed lines represent the first four anti-crossings for this state, which correspond to the first four abrupt changes in S_A in Fig. 6(c). Right plots: zoom into the first four anti-crossings of the $N/2$ -th state.